Plasmonics (2020) 15:609–621
https://doi.org/10.1007/s11468-019-01071-z

Design of Aluminum Bowtie Nanoantenna Array with Geometrical Control to Tune LSPR from UV to Near-IR for Optical Sensing

Bin Wang [1,2] · Subhash C. Singh [1,3] · Huanyu Lu [1,2] · Chunlei Guo [1,3]

Received: 14 July 2019 / Accepted: 3 November 2019 / Published online: 27 November 2019

Abstract

Plasmonic nanoantennas have earned strong recognition for their unique capability to confine light from free space into sub-wavelength dimensions with strong electric field (E-field) enhancement factor due to localized surface plasmon resonance (LSPR). Broad spectral tuning of LSPR from ultraviolet (UV) to near-infrared (NIR) is required for incident light wavelength and material sensitive plasmonic applications in different spectral regions. In this article, we introduced and designed a novel aluminum plasmonic platform consisting of a bowtie nanoantenna (BNA) array with metal-insulator-metal (MIM) configuration where LSPR peak position was broadband tunable from UV to NIR through geometric control of antenna parameters. Furthermore, we designed and numerically analyzed a plasmonic biosensor platform that detected concentration of glycerol in de-ionized (DI) water with a concentration in the range of 0 to 40 wt% (refractive index = 1.333 to 1.368) with a sensitivity of 497 nm/RIU (refractive index units). The designed plasmonic platform can also be used as a surface-enhanced Raman scatting (SERS) substrate with enhancement factor as high as 4.82×10^9 for 1042 nm excitation wavelength. The reported hybrid dielectric-metallic plasmonic nanostructured system is a universal plasmonic platform for a wide range of applications including single-molecule SERS, biosensing, fluorescence microscopy, plasmonic nanocavity, nanolasers, and solid-state lighting.

Keywords Aluminum plasmonics · Bowtie nanoantenna · Localized surface plasmon resonance · Tunability · SERS · Plasmonic sensor

Introduction

Recently, plasmonic nanoantennas received enough attention owing their unique capability to confine light from free space into sub-wavelength dimensions with strong electric field (E-field) enhancement due to localized surface plasmon resonance (LSPR) [1–11]. Various designs of plasmonic nanoantennas such as Yagi-Uda antennas, spiral nanoantennas, honey-comb antennas, nanodiscs, nanorods, and bowtie antennas with LSPR wavelengths ranging from ultraviolet (UV) to near-infrared (NIR) spectral regions are used for a number of optical and sensing applications, including but not limited to surface-enhanced Raman scattering (SERS) [12–15], single-molecule detection [16–18], biosensing [19, 20], and nanoscale light sources [21, 22]. The triangular geometry of bowtie nanoantenna (BNA) in particular can strongly confine E-field in a very small gap region through the in-plane near-field coupling or the in-plane far-field coupling [9, 11, 23–28]. The spectral response and E-field enhancement factor (EF) of BNA can be tuned through the engineering of their geometrical parameters [29–31].

Material selection for the fabrication of plasmonic structures is crucial for the practical realization of low-cost and environmentally durable plasmonic devices. Typically, noble metals such as gold and silver are the most common materials used to fabricate plasmonic structures for visible and NIR applications [32, 33]. LSPR from gold is durable due to its chemical inertness, while silver reacts with atmospheric sulfur and oxygen that degrade its plasmonic properties over time [34]. These metals not only are costly but also have limitations

Electronic supplementary material The online version of this article (https://doi.org/10.1007/s11468-019-01071-z) contains supplementary material, which is available to authorized users.

✉ Subhash C. Singh
ssingh49@ur.rochester.edu

✉ Chunlei Guo
guo@optics.rochester.edu

[1] Changchun Institute of Optics, Fine Mechanics and Physics, Chinese Academy of Sciences, Changchun 130033, China

[2] University of Chinese Academy of Sciences, Beijing 100049, China

[3] The Institute of Optics, University of Rochester, Rochester, NY 14627, USA

on LSPR tunability due to their intrinsic absorption. For example, gold and silver have intrinsic absorptions around 500 and 400 nm, respectively, restricting their applications in the UV spectral range [35]. Aluminum (Al) is an inexpensive and abundant earth metal with a high plasma frequency that enables its application in the UV and deep UV spectral regions [36, 37]. Moreover, the natural growth of a thin 3–5-nm self-terminating oxide layer on its surface protects the underlying bulk metal from further oxidation, making Al the most suitable choice for the fabrication of cheap, durable, and robust plasmonic devices [38]. Due to its compatibility with complementary metal-oxide semiconductor (CMOS) technology, Al plasmonic nanostructures can be directly integrated with silicon photonics for the fabrication of lab-on-chip plasmonic devices, waveguides and interconnects, biosensors, etc. [39].

The tuning of LSPR from UV to NIR spectral region is required for different plasmonic applications. For example, LSPR in the UV-visible spectral range is required for optical biosensing, solar energy harvesting, SERS, UV-visible spectroscopy, photodetection, UV plasmonic lasing, plasmonic waveguide, etc., while LSPR in the NIR range is useful for biomedical applications, thermal imaging, and fabrication of IR light sources and IR detectors. In general, different materials or different geometric structures are required to tune LSPR in the different spectral regions that pose material-dependent fabrication/design challenges. Most of the previous reports use noble metals for plasmonic applications. For example, in reference [11], the authors reported the gold bowtie antenna with metal-insulator-metal (MIM) structure and only studied the effects of spacer thickness on the absorption and scattering coefficients. However, most of reported applications on the Al plasmonic structures were limited in the UV and deep UV spectral region [6, 36, 38].

Herein, we designed a range of Al BNA with MIM configurations and dealed a much-detailed study on their optical response influenced by geometric and optical parameters numerically in the UV-visible-NIR spectral region. The geometric parameters of BNA including gap distance (g), period (P), antenna side length (L), antenna thickness (Z), antenna angle (θ), and thickness of the insulating layer (T) were varied to tune LSPR position from UV to NIR spectral regions. For a geometrically optimized antenna, the influences of incident angle and light polarization on the LSPR peak position and E-field EF ($|E|/|E_0|$) were studied. Our BNA designed with MIM structure can enhance E-field by a factor of 100, which is about ten times larger than the previous BNA structure with similar gap sizes [40, 41]. Following this MIM strategy, we designed BNA with a gap of 10 nm and a side length of 360 nm, resulting in SERS EF ($|E|/|E_0|^4$) as high as 4.82×10^9 at 1042 nm near the tips of antennas and in the gap region. Such types of substrates could be used for single-molecule detection using SERS and single-photon detection through strong coupling between an emitter placed in the gap and a far-field single-photon radiation source [42]. Ultimately, we simulated the plasmonic behavior of BNA in the presence of external stimuli for their potential application as an inexpensive refractive index–based biosensor. The refractive index of the antenna environment was numerically changed in the range of 1.333 to 1.368, equivalent to 0 to 40% concentration of glycerol in the de-ionized (DI) water [19], and the corresponding shift in the LSPR peak position is calculated. The sensitivity of our MIM-based plasmonic BNA biosensor is roughly ~ 500 nm/RIU.

Design of BNA and FDTD Simulation

The plasmonic nanostructure surface (schematically shown in Fig. 1a) consists of an array of periodic Al BNA above a 100-nm-thick Al film deposited on the glass substrate. In a MIM (Al-SiO_2-Al) configuration, the BNA array is separated from the Al film by a thin SiO_2 spacer. Figure 1 b and c show front and the top views of the plasmonic structure, respectively. The geometric parameters of the Al BNA array, shown in Fig. 1 b and c, such as gap distance (g) (defined as the distance along the y-axis between the tips of BNA), period (P) (defined as distance along the x-axis between the tips of BNA), antenna side length (L), antenna thickness (Z), antenna angle (θ), and thickness of the insulating layer (T), are numerically changed to tune the LSPR peak position from UV to NIR spectral region. To study the dependence of LSPR peak position and E-field EF on BNA array parameters (g, P, L, Z, θ, and T) and refractive index of the antenna environment for the given BNA parameters, we employed the finite difference time domain (FDTD) method based on Yee's algorithms. In the FDTD method, Maxwell's equations are discretized in both time and space, and central difference approximation is used. A commercial FDTD package known as Lumerical solutions (Lumerical Inc.) was used to calculate the spectral response of E-field distribution at the center of the gap in the spectral range of 200 to 2000 nm. The plasmonic structure with BNA array was normally illuminated from a broadband (λ 200–2000 nm) plane wave light source having electric field oscillation along the y-axis (antenna orientation direction) (Fig. 1a). Two detector boxes were used to measure the spectral response. The periodic boundary condition was used in the x-direction, while the perfect matching layers (PML) were used in the z- and y-directions (Figs. 3f and 8a). The time monitors were used to detect the change in the electric field over time. An ultrafine 1-nm mesh size was used in all simulations. A refractive index of $n_{sup} = 1.0$ was chosen for air to generate an asymmetric environment while indices for Al and SiO_2 were obtained by dispersion relation provided by Palik. For the given geometric parameters of BNA array, the angle of incidence and polarization orientation of the electromagnetic field were also swept to understand their dependence on LSPR peak position and E-field EF. For a given BNA parameter, the effective index of

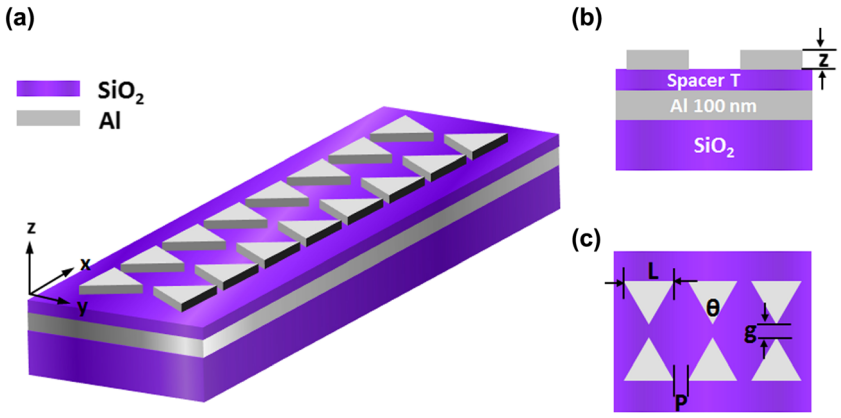

Fig. 1 **a** Schematic of the Al BNA array with MIM configuration. **b** Front and **c** top views of BNA. An Al thin film is sandwiched between the spacer layer and the SiO_2 substrate. The thickness of the Al thin film is set as 100 nm, which totally blocks the light transmission through the structure

antenna environment was numerically changed in the range of 1.33 to 1.95 and spectral reflectance was simulated for normal incidence to understand the applicability of these BNA structures as inexpensive refractive index sensors. The absorbed power was calculated by $P = -0.5\omega|E|^2\,\mathrm{Im}(\varepsilon)$, where $\omega = 2\pi f$, f is the frequency of the light, $|E|^2$ is the electric field intensity, and $\mathrm{Im}(\varepsilon)$ is imaginary part of the dielectric function [11].

Results and Discussion

Firstly, we studied the effects of MIM configuration on the spectral response of E-field enhancement (Fig. 2a). We chose a reference point P_0 at the center position of the gap and calculated the E-field enhancement ($|E|/|E_0|$) at this point. There are three modes of LSPR shown in Fig. 2b. The first mode ($LSPR_1$), located at 970 nm, is the primary mode corresponding to the dipolar LSPR mode. The E-field resulting from LSPR coupling between closely spaced nanoprisms is localized in the bowtie gap. The two higher-order LSPR modes located at 369 nm ($LSPR_2$) and 232 nm ($LSPR_3$) are due to the localization of E-field into the gap and the edges or outer corners of nanoprisms, respectively [43]. Due to the higher intensity of $LSPR_1$ mode relative to the other two, we only considered the impact of $LSPR_1$ mode in the present study. It is interesting to note that with the use of MIM configuration, the E-field intensity of $LSPR_1$ mode gets doubled, while its fullwidth at half-maxima (FWHM), $\Delta\lambda$, gets nearly halved (Fig. 2b). These changes in the LSPR characteristics enhance its quality factor ($QF = \lambda_0/\Delta\lambda$; where λ_0 is LSPR peak position) by more than fourfold. Figure 2 c and d show the spatial distribution of E-field at 970 nm wavelength in the x-y plane without and with the MIM configurations, respectively. It is clear from these data that the use of a MIM configuration results in significantly stronger E-field EF (Fig. 2b) and a larger spatial distribution (Fig. 2d) for LSPR mode in the gap region. The use of an Al metal layer in the MIM structure strongly reflects light and confines wavelength corresponding to LSPR in the gap region, resulting in strong light absorption in the structure [44].

The dimensions (geometry) of the BNA, including gap distance (g), period (P), antenna side length (L), antenna thickness (Z), and thickness of the insulating layer (T), are tuned to control the position of LSPR absorption and E-field EF (Fig. 3). We have chosen $L = 120$ nm, $Z = 60$ nm, $P = 20$ nm, $g = 10$ nm, and $T = 20$ nm for the BNA array and then simulated E-field at the reference point P_0 (Fig. 2a). Accompanying each graph in Fig. 3 is a schematic sketch of BNA with a parameter that is swept. The swept geometrical parameter is indicated on the x-axis. To understand the effects of variation in L on the LSPR peak position and E-field EF, we swept L in the range of 40–300 nm while keeping other parameters ($Z = 60$ nm, $P = 20$ nm, $g = 10$ nm, and $T = 20$ nm) constant. When the L of BNA is increased from 40 to 300 nm, the LSPR peak position has a longer wavelength shift with comparatively higher E-field EF as shown in Fig. 3a (full spectrum see Fig. S1a). This corresponds to the dipolar LSPR mode which demonstrates a longer wavelength shift when the side length of the triangle is increased [45]. In a similar fashion, we swept BNA's Z in the range of 20 to 150 nm while keeping other parameters ($L = 120$ nm, $P = 20$ nm, $g = 10$ nm, and $T = 20$ nm) constant. We can see that increasing the Z of the BNA also causes longer wavelength shift in the LSPR peak position but decreases the E-field EF (full spectrum, see Fig. S1b). This is due to the delocalization of charge density at the apex, which increases with the increase in the height [46].

Next, we investigated the effects of variation in the g and P values on the LSPR and E-field EF response of BNA (Fig. 3c, d). Increasing the g from 10 to 80 nm initially causes a fast smaller wavelength shift in the LSPR peak position (1050 to 1010 nm with change in g from 10 to 30 nm), followed by a slower (1010 to 990 nm with change in g from 30 to 80 nm) wavelength shift towards shorter wavelength side and finally attaining a constant value at $g \geq 80$ nm (Fig. 3c; full-spectrum, see Fig. S1c). Macroscopically, the LSPR peak position is nearly fixed around 1000 nm. It is well-established that the

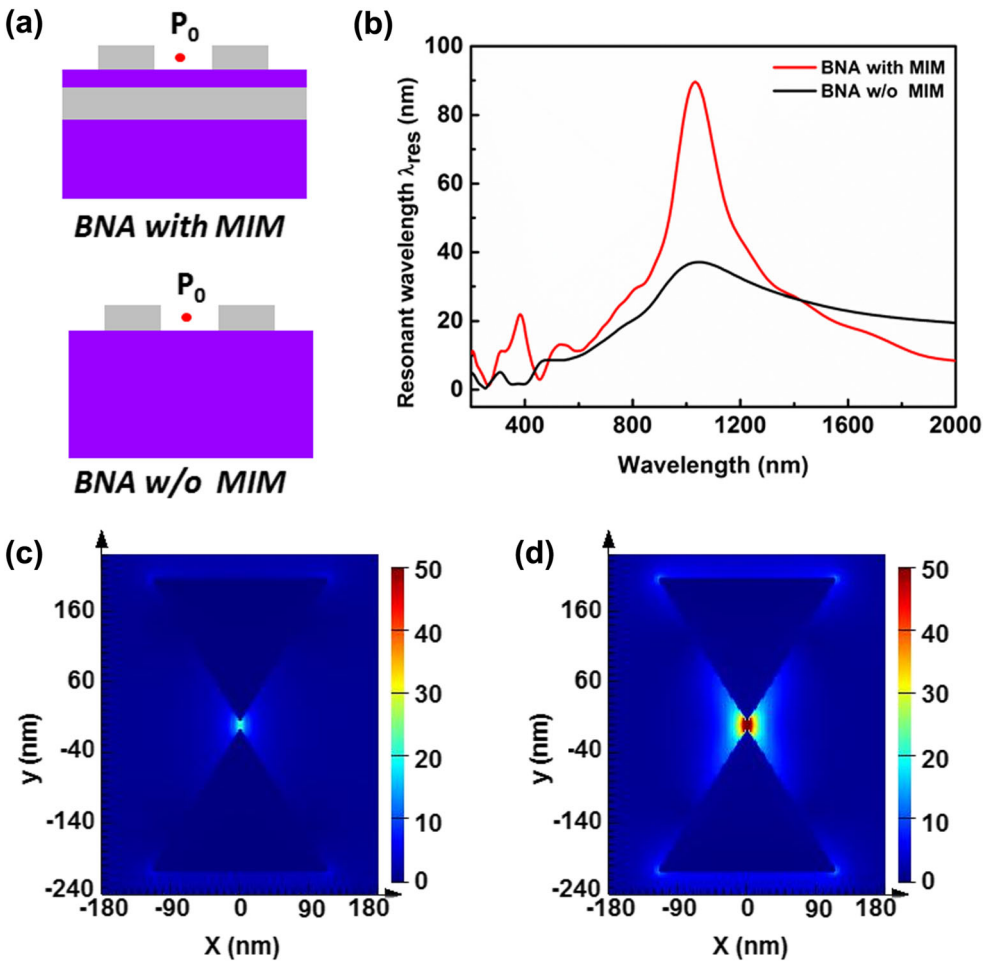

Fig. 2 **a** Schematic of the Al BNA with and without MIM configuration. **b** E-field enhancement of BNA with and without MIM configuration. E-field distribution of BNA **c** without and **d** with MIM configuration at $\lambda = 970$ nm in the *x*-*y* plane

narrower the gap size, the stronger the E-field confinement. E-field EF shows almost $1/r^2$ dependence on the g that is in accordance with the classical electrostatics (Fig. 3c). The period (P) of a BNA array determines cross-talk between two pairs of BNA and hence charge localization and E-field distribution in the space of the period. As the period of antenna increases, the interaction between neighboring nanoantennas will decrease, which will influence the LSPR peak position and E-field EF in the gap region [47, 48]. As shown in Fig. 3d, the period of BNA array is tuned from 0 to 720 nm to control LSPR peak position and E-field EF of plasmonic structure. It is interesting to note that LSPR peak position shifts towards shorter wavelength until P is larger than 400 nm and attains a plateau. In the range of study, E-field EF increases almost linearly with the increase in the period (full spectrum, see Fig. S1d). From these results, we can conclude that parameters of g and P primarily influence the E-field intensity enhancement and have less influence on the LSPR peak position.

Using the MIM structure, which can engineer both out-of-plane and in-plane near-field couplings to tune the far-field coupling [11], we can achieve maximized E-field EF in the bowtie gap region with increased spectral response. Therefore, the parameters of the MIM structure need to be optimized. Varying T from 5 to 50 nm, the LSPR peak position showed a smaller wavelength shift from 1250 to 1000 nm and a slight increase in E-field EF from 25 to 35 (Fig. 3e; full-spectrum, see Fig. S1e). This out-of-plane coupling caused by MIM structure can be attributed to the near-field interaction between the BNA and its image in the Al film [49]. Since the E-field was confined in the spacer, therefore, increase in the spacer thickness causes a decrease in the out-of-plane coupling strength in the spacer that results in a shorter wavelength shift in the LSPR peak position. Figure 3 f shows the setting of boundary conditions, light source, and monitors as described in the second part of the model design.

Furthermore, the influence of the bow angle, θ, on the LSPR peak position and E-field EF of the designed structure has been also analyzed. For BNA, a triangle with a fixed height of 175 nm was chosen while its side length was swept from 100 to 650 nm to vary the bow angle (θ) in the range of 46° to 120° (Table 1). We chosen fixed parameters of $g =$ 10 nm, $Z = 60$ nm, $T = 20$ nm, and $P = 20$ nm with normal illumination from a plane wave light source with electric field oscillation along the y-axis (antenna orientation direction).

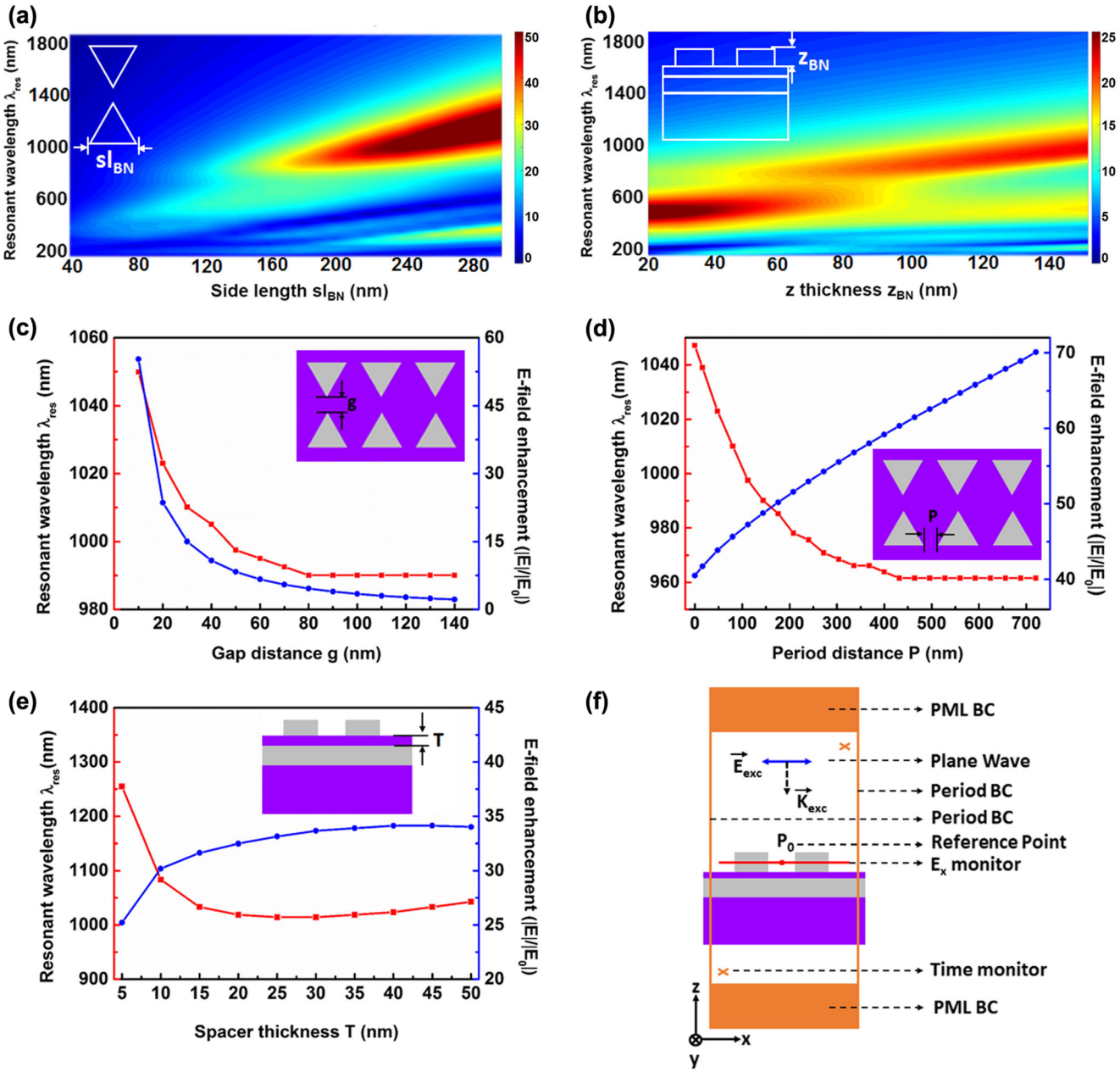

Fig. 3 LSPR peak wavelength and E-field intensity enhancement ($|E|/|E_0|$) of BNA array with MIM configuration as a function of **a** side length (L), **b** thickness (Z), **c** gap distance (g), **d** period distance (P), and **e** spacer thickness (T). **f** The schematic for source and monitor positions with respect to structure. The blue dash line and the red line in **c**–**e** show the change of the E-field intensity enhancement ($|E|/|E_0|$) and resonant wavelength with different parameters, respectively. The inset pictures in all the figures show the different changing parameters

Figure 4 a gives the spectral response for different bow angles in the range of $46° \le \theta \le 120°$. To analyze the relationship between spectral response and bow angle, we extracted two sets of data, one for $46° \le \theta \le 98°$ (Fig. 4b) and another for $98° \le \theta \le 120°$ (Fig. 4c). It is clear from Fig. 4b that the E-field intensity is enhanced dramatically, from 40 to 90, as bow angle is increased from 46 to 98°; however, the LSPR peak position remains relatively stable around 1042 nm. However, change in bow angle from 98 to 120° results strong redshift in the LSPR peak position with relatively little change in the E-field EF (Fig. 4c). This situation can be attributed to the

Table 1 Bow angle θ: acute angle to obtuse angle

L (nm)	150	200	250	300	350	400	450	500	550	600
θ (°)	46	60	71	81	90	98	104	110	115	120

Bow angle θ of the triangle from 46 to 120° by changing the side length from 100 to 650 nm with a fixed triangle height of 175 nm

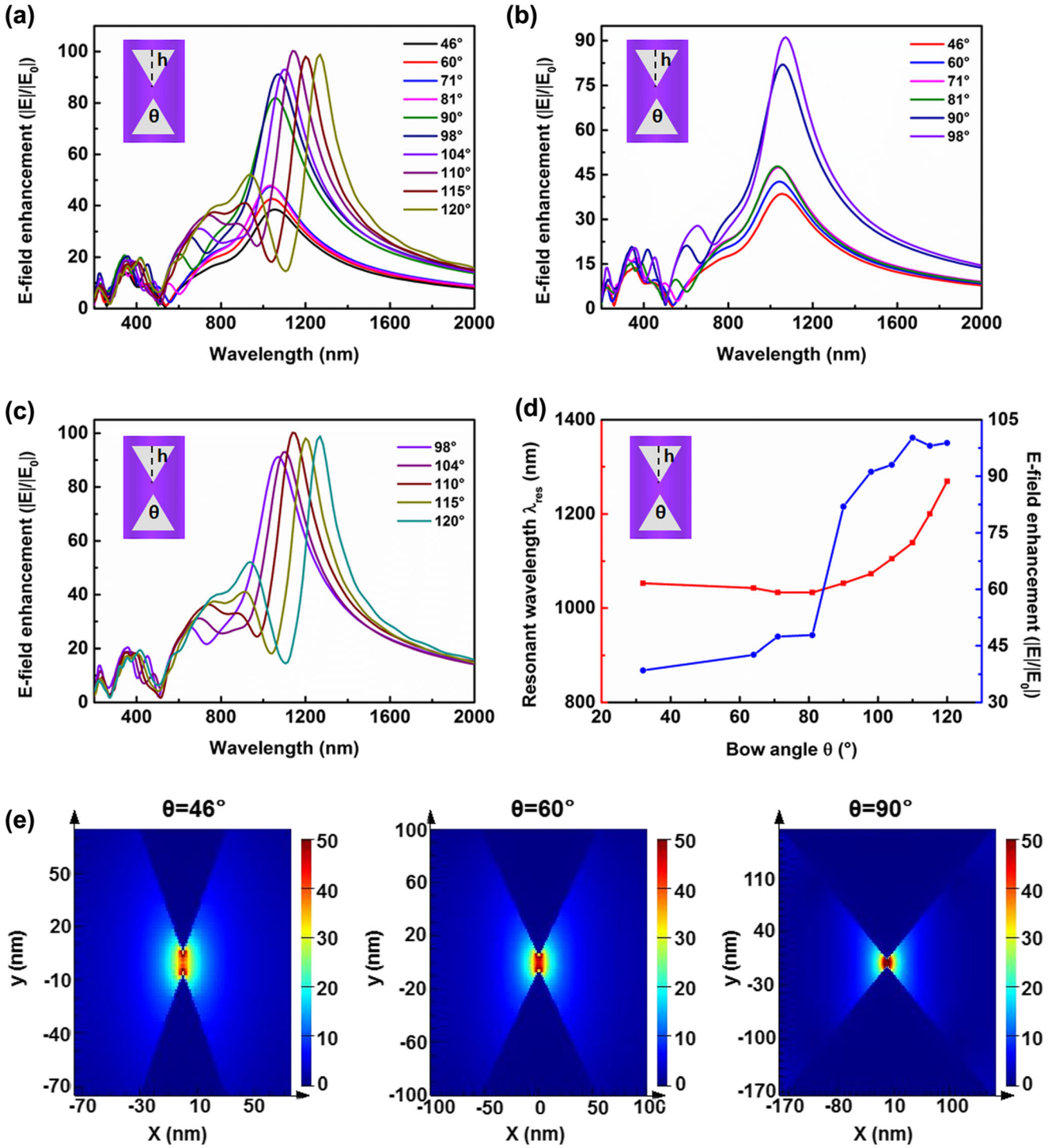

Fig. 4 **a** The spectrum response of the BNA with θ from 46 to 120°. **b**, **c** The spectrum response of the BNA with θ from 46 to 98° and θ from 98 to 120°. **d** The maximum LSPR peak wavelength and E-field intensity enhancement as a function of changing the bow angle from 32 to 120°. **e** E-field distributions of the BNA with 46°, 60°, and 90° bow angle at a wavelength of 1042 nm in the *x*-*y* plane. The gap size of the bowtie nanoantenna is 10 nm

change in the effective index of the local surface plasmon polariton (SPP) [50–52]. As the bow angle increased, the lateral dimension of the nanoantenna becomes larger, resulting in a decrease of the effective index of the local SPP. For small bow angles, the standing SPP wave is established along the antenna axis, but for very large bow angles, the local SPP is confined at one air/Al interface and is not affected by the opposing interface, especially when the cross section is close to the extremity edges. In such cases, the isolated local SPPs propagate back and forth along the prism edges, interfere, and

give rise to a standing wave whose resonant wavelength is proportional to the length of the prism edges. This results in a longer wavelength shift for a large increase in the bow angle. From these results, we can conclude that the E-field EF and LSPR peak positions can be independently controlled by varying bow angle in two different θ ranges. The variations in LSPR peak position and E-field EF as a function bow angle are shown in Fig. 4d. Figure 4 e presents the spatial distribution of E-field around the BNA in the *x-y* plane for 32°, 60°, and 90° bow angles at a fixed wavelength of 1042 nm.

After studying the effects of geometric parameters of BNA on spectral E-field response, the effects of

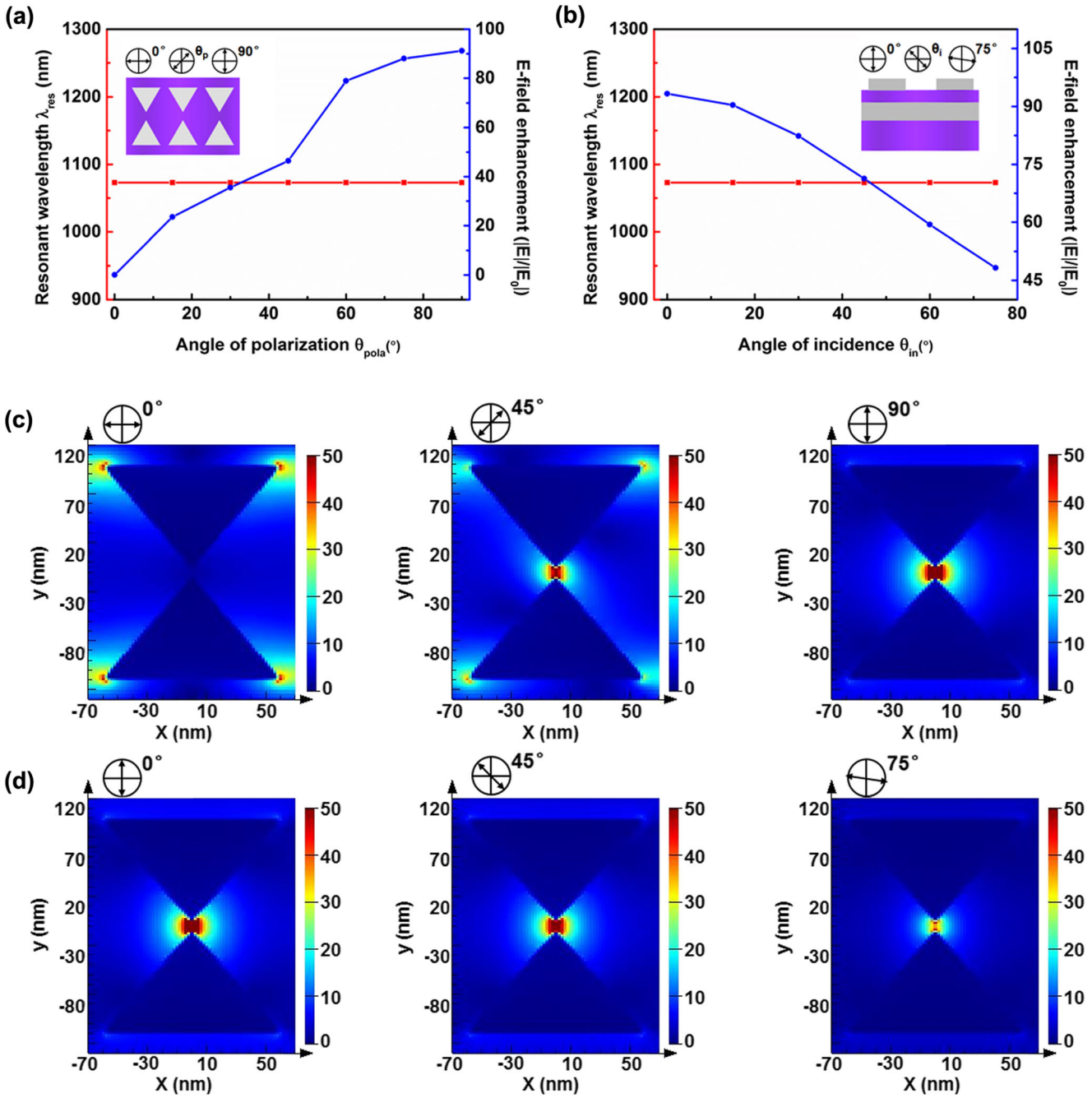

Fig. 5 LSPR peak wavelength and E-field intensity enhancement ($|E|/|E_0|$) of the BNA array with MIM configuration as a function of **a** polarization angle and **b** incident light angle. **c** E-field distributions of the BNA array with 0°, 45°, and 90° polarization angle at a wavelength of 1064 nm. **d** E-field distributions of the BNA array with 0°, 45°, and 75° incident light angle at a wavelength of 1064 nm. The gap size of the BNA is 10 nm. E-field distributions are shown in *x-y* plane

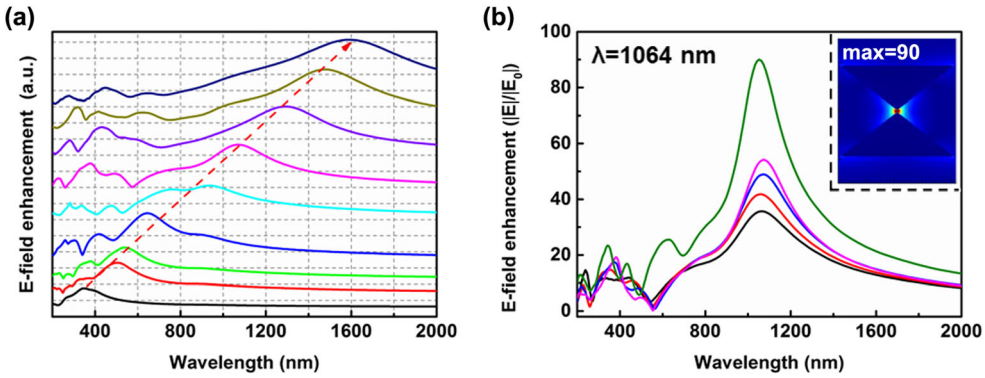

Fig. 6 **a** Engineering spectrum response from UV to NIR at different structure parameters. The spectra are shifted relative to one another along the *y*-axis for ease of viewing. **b** Increasing E-field intensity enhancement ($|E|/|E_0|$) from 35.68 to 89 at 1064 nm. The insert figure is the E-field distribution of BNA which has the highest enhancement of ~ 89 (olive curve)

incident light source parameters, such as an angle of incidence (θ_{in}) and polarization (θ_{pola}), on the spectral response of a given BNA are simulated (Fig. 5). The schematic accompanying the graphs shows the direction of θ_{in} and θ_{pola}. The LSPR peak position is found independent on the angle of incidence and polarization, but the E-field EF depends on these source parameters. As shown in Fig. 5a, E-field intensity enhancement shows an obvious increase as the angle of polarization increased, reaching its maximum value for $\theta_{pola} = 90°$ (full spectrum, see Fig. S2a). Figure 5 c shows that the E-field distribution is mainly localized at four non-gap vertices of triangles for $\theta_{pola} = 0°$, but the gap region nearly has no enhancement. When the polarization of incident light is changed to 45°, the E-field is distributed throughout the whole structure and has large enhancement around the tip and gap region of the BNAs. For 90° polarization (along the *y*-axis), the E-field localized in the gap region and has the largest enhancement compared with other situation.

Figure 5 b shows the LSPR peak position and the E-field EF as a function of incident light angle θ_{in} at the reference point P_0. Very similar to the angle of polarization, angle of incidence does not affect the LSPR peak position, but E-field EF significantly decreases from 93 to 48 with an increase in the θ_{in} from 0 to 75° (full spectrum, see Fig. S2b). We can also see from Fig. 5d that the spatial distribution of E-field in the gap region of BNA decreases with an increase in the θ_{in} from 0 to 75°. From these results, we can say that the E-field EF can be independently controlled by changing the light source parameters such as angle-of-incidence and polarization at a given wavelength.

From the above analysis, we know that the optical response of plasmonic nanoantennas can be engineered through optimizing the parameters of Al BNA with MIM structure and the angles of light source's incidence and polarization. Therefore, it is possible to achieve tunable LSPR wavelength from UV to NIR spectral region using a plasmonic cavity with Al BNA array combined with a MIM sandwich structure using different geometrical parameters as shown in Fig. 6a. The spectra are shifted relative to one another along the *y*-axis for ease of viewing. Table 2 shows the geometric parameters at different resonant wavelengths using the same angles of $\theta_{in} = 0°$ and $\theta_{pola} = 90°$. It is worth to note that the spectral response with various structural parameters (Fig. 6a) is not optimal for the current parameters (Table 2), which means that they do not achieve the maximum E-field EF. The current research investigates the property of Al BNA array with MIM structure, which can change the LSPR peak position from UV to NIR region by engineering geometric parameters. For a given LSPR peak position $\lambda_{res} = 1064$ nm, we can increase E-field EF from ~ 35 to ~ 89 by changing different geometrical parameters (Fig. 6b). Table 3 gives the structural parameters of different E-field EF intensities at $\lambda_{res} = 1064$ nm for a given light source ($\theta_{in} = 0°$ and

Table 2 Structure parameters with different LSPR peak wavelengths

	black	red	green	blue	cyan	magenta	valet	yellow	navy
λ_{res} (nm)	346	481	532	640	800	1064	1310	1470	1600
sl_{BN} (nm)	50	160	180	240	260	220	280	240	300
Z_{BN} (nm)	20	25	30	40	55	60	100	150	140
θ_{bow} (nm)	60°	98°	98°	98°	90°	60°	60°	60°	60°

Structure parameters at different LSPR peak wavelengths according to curves of different colors shown in Fig. 6a

Table 3 Structure parameters with different $|E|/|E_0|$ at $\lambda_{res} = 1064$ nm

	black	red	blue	magenta	olive
λ_{res}	1064 nm	1064 nm	1064 nm	1064 nm	1064 nm
E/E_0	35.68	41.80	48.94	54.18	89.01
sl_{BN}	180 nm	200 nm	220 nm	230 nm	360 nm
Z_{BN}	90 nm	70 nm	55 nm	40 nm	40 nm
θ_{bow}	60°	60°	60°	60°	90°

Structure parameters with different $|E|/|E_0|$ at λ_{res}=1064 nm according to curves of different colors shown in Fig. 6b

$\theta_{pola} = 90°$) parameters. The Al BNA array with MIM structure can provide highly focused optical energy and an E-field EF-enhancing plasmonic cavity with a tunable resonant wavelength from UV to NIR spectral region and support many applications in these optical regions.

Applications of BNA in Optical Sensing

SERS SERS is an ultrasensitive chemical-sensing technique capable of single-molecule detection [53–55]. The strong enhancement is mainly the result of electromagnetic enhancement which occurs due to the LSPR of noble metal nanoparticles (NPs) or surface plasmon resonance (SPR) of metallic thin films onto which the target molecules are adsorbed [56–58]. Since the SERS enhancement factor (EF) is proportional to $|E|/|E_0|^4$ [59, 60], where $|E|$ and $|E_0|$ are the magnitude of the exciting electric field in the vicinity of the plasmonic nanostructures and incident electric near field, respectively, therefore the strong SERS enhancement occurs at the locations of "hot spots" having maximum E-field EF.

In this section, we designed BNA with geometric parameters as $L = 360$ nm, $g = 10$ nm, $P = 1080$ nm, $T = 20$ nm, $Z = 40$ nm, and $\theta = 90°$. Raman spectroscopy mostly works in the back reflection geometry, where the excitation light is normally incident on substrate and Raman signal is collected in backscattering geometry. Therefore, here we used normal incidence light source of $\lambda = 1042$ nm with polarization along the antenna direction ($\theta_{in} = 0°$ and $\theta_{pola} = 90°$) and put monitor (detector) at the normal of the substrate. As shown in Fig. 7 a and b, E-field EF varies with distance from the center of the gap (reference point). At a given height, $Z = 20$ nm (middle of

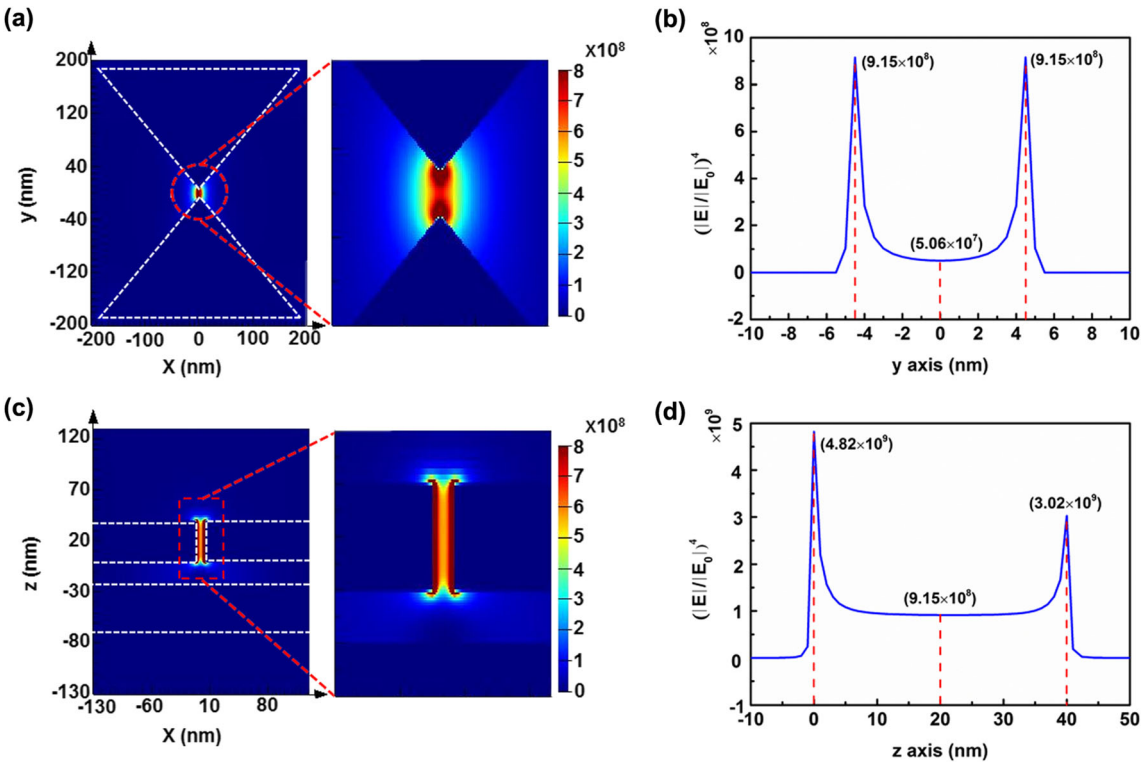

Fig. 7 E-field intensity distribution ($|E/E_0|^4$) of induced localized electrical field E relative to the excitation field E_0 at 1042 nm in **a** *x*-*y* plane and **c** *y*-*z* plane. The E-field intensity distribution ($|E/E_0|^4$) in the gaps as a function of distance from the center of the gap along **b** *y*-axis and **d** *z*-axis

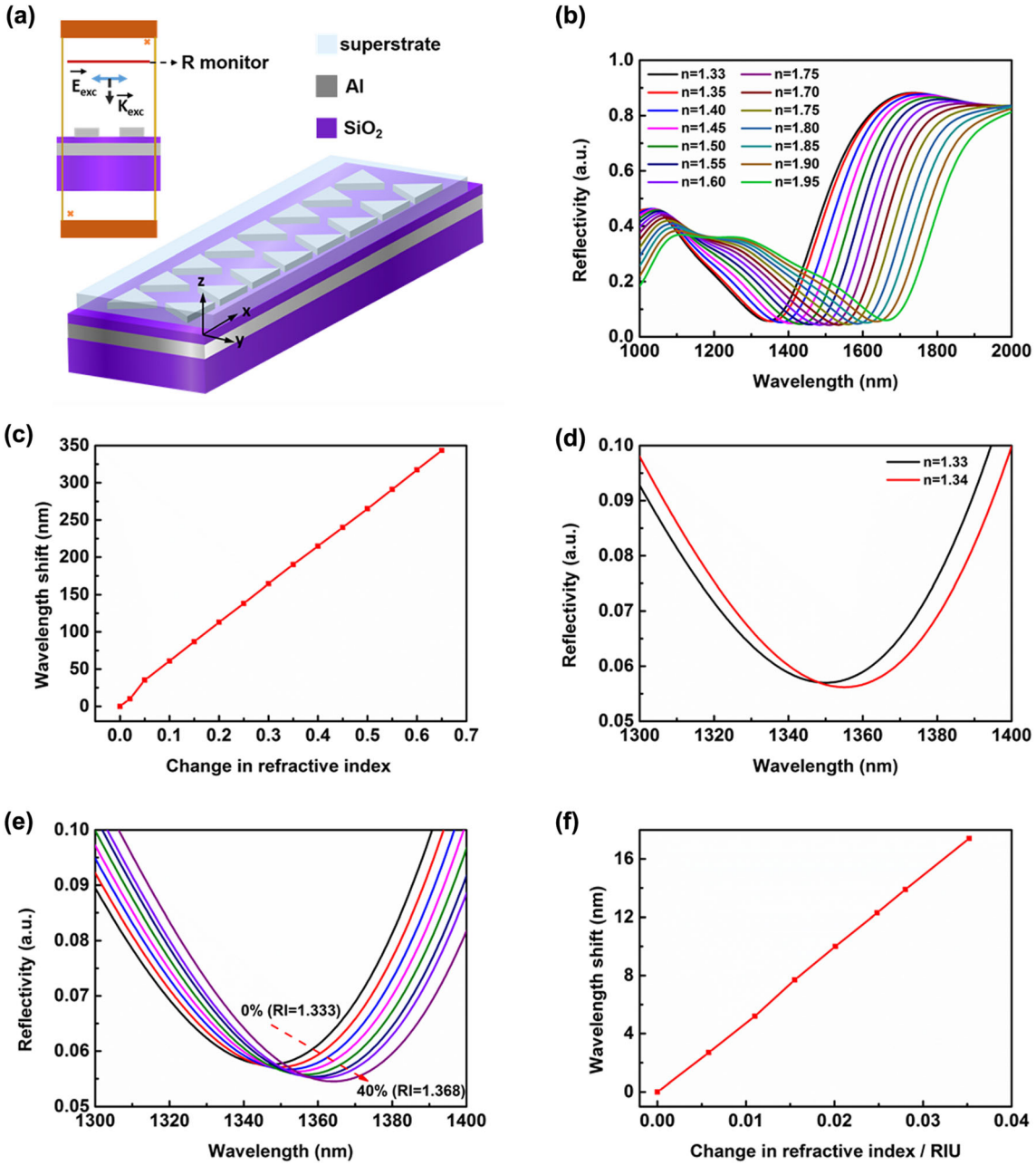

Fig. 8 **a** Schematic and computational model of the bio-sensing platform consists of Al BNA array with a MIM structure. **b** Normalized reflectance spectra of the functionalized BNA as a function of the substrate refractive index ranging from 1.33 to 1.95. **c** The variation of wavelength shift with a change in refractive index. **d** Zoom-in reflection spectra of the BNA when superstrate refractive index changes from 1.33 to 1.34. **e** Normalized reflectance spectra for different concentrations of glycerol in DI water (0%–40 wt%/RI = 1.333–1.368). **f** The variation of wavelength shift with different concentrations of glycerol in DI water

the triangle of $Z = 40$ nm), the maximum SERS EF ($|E|/|E_0|^4$) localized on the two tips of BNA is $\sim 9.15 \times 10^8$. A comparatively smaller but more uniform enhancement factor of $\sim 5.06 \times 10^7$ has resulted in the gap region (Fig. 7b). For a given y, SERS EF spatially varies in the z-direction (Fig. 7c, d). For example, at the tip of BNA ($y = 4.5$ nm), SERS has maximum EF of $\sim 4.82 \times 10^9$ at the bottom of tip ($z = 0$ nm), $\sim 3 \times 10^9$ at the top ($z = 40$ nm), and has a comparatively lower but uniform value of $\sim 9.15 \times 10^8$ in the region of $5 \le z \le 35$ nm. Through an intelligent design of Al BNA, the LSPR peak positions can be tuned from UV to NIR to wavelength match with the wide range of available laser sources [61] for high sensitivity SERS detection of wavelength sensitive probe molecules.

High Sensitivity Bio-sensing Platform The theoretical essence of plasmonic biosensors is the coupling between the electromagnetic field and confined free electrons in space, which can effectively improve the sensitivity of LSPR optical antenna biosensors and achieve high-resolution, nanoscale biomolecule detection [62–64]. When the wave vector of incident light satisfies the resonant condition, the extinction coefficient of nanoantennas will reach its maximum value. The sensitivity of resonance frequency depends on the refractive index of the surrounding medium and the size and shape of nanoantennas at a given wavelength [20, 65, 66]. Plasmonic sensors, therefore, facilitate the high-performance detection of the change in the refractive index resulting from biomolecular reactions and can be used to study the nature of such interactions.

In this section, we numerically designed and analyzed a high-performance bio-sensing platform based on BNA, which could sense the change in the medium refractive index (RI) caused by the density of probe molecules in the vicinity of the plasmonic structure. For this purpose, we chose the BNA structure with geometric parameters of $L = 300$ nm, $Z = 60$ nm, and $g = 10$ nm. We used a normal incident light source and put a reflection monitor in the 180° (back reflection geometry) configuration. Figure 8 a shows a schematic of the designed structure and position of source and monitor. The superstrate is put over the entire BNA array to change the RI of the BNA environment. We numerically changed the effective index of the antenna environment from 1.33 to 1.95 and simulated the reflected optical signal. Figure 8 b presents normalized reflection spectra for different refractive indices. Figure 8 c shows an almost linear shift in the LSPR peak position with the refractive index with the slope of ~ 500 nm/RIU. When RI is changed from 1.33 to 1.34, a 1% change in RI, there is a ~ 5.5 nm wavelength shift as shown in Fig. 8d. For comparison with a real case scenario, the concentration of glycerol in de-ionized (DI) water is numerically varied from 0 to 40% (w/w) which is equivalent to the change in the effective index of the antenna medium from 1.333 to 1.368. As shown in Fig. 8e, LSPR peak position experiences a longer wavelength shift when the concentration of glycerol in DI water is changed from 0 to 40 wt% (RI = 1.333 to 1.368) [19]. Figure 8 f shows the sensitivity of the LSPR peak position as measured in wavelength shift with the change in the concentration of glycerol in the DI water. When the concentration is 40%, a 17.4 nm shift is observed with a maximum sensitivity of 497 nm/RIU (refractive index units) at peak wavelength.

Conclusion

With the capability to efficiently convert light from free space into the sub-wavelength scale and vice versa, plasmonic nanoantennas find a wide range of applications in nanophotonics. The influences of geometric parameters of Al BNA with MIM configuration and angles of incidence and polarization of light source are studied in detail. By optimizing geometric parameters of Al BNA array with MIM structure, the LSPR of plasmonic nanoantennas can be tuned from UV to NIR spectral region, 200 to 2000 nm, with highly enhanced E-field intensity in the gap region. Further, by controlling the angles of incidence and polarization of the light source, E-field distribution and intensity can also be manipulated. Moreover, we numerically analyzed the sensitivity of these plasmonic structures as SERS substrates and refractive index–based biosensors. An optimized structure can achieve SERS enhancement factor ($|E|/|E_0|^4$) as high as 4.82×10^9 and can be efficiently used as a refractive index sensor with sensitivity ~ 497 nm/RIU. We believe that the designed hybrid dielectric-metallic nanostructure can be used in a wide range of plasmonic applications including but not limited to single-molecule SERS, biosensing, fluorescence microscopy, plasmonic nanocavity, nanolaser, and solid-state lighting.

Funding Information Scientific Research Project of the Chinese Academy of Sciences (QYZDB-SSW-SYS038); National Natural Science Foundation of China (11774340); and the Open Fund of the State Key Laboratory on Integrated Optoelectronics (No. 2015IOSKL).

References

1. Novotny L, Van Hulst N (2011) Antennas for light. Nat Photonics 5(2):83–90
2. Sundaramurthy A, Crozier KB, Kino GS et al (2005) Field enhancement and gap-dependent resonance in a system of two opposing tip-to-tip Au nanotriangles. Phys Rev B 72(16):162409
3. Merlein J, Kahl M, Zuschlag A et al (2008) Nanomechanical control of an optical antenna. Nat Photonics 2(4):230–233
4. Casadei A, Pecora EF, Trevino J, Forestiere C, Rüffer D, Russo-Averchi E, Matteini F, Tutuncuoglu G, Heiss M, Fontcuberta i Morral A, Dal Negro L (2014) Photonic-plasmonic coupling of GaAs single nanowires to optical nanoantennas. Nano Lett 14(5): 2271–2278
5. Abb M, Wang Y, Papasimakis N, de Groot CH, Muskens OL (2014) Surface-enhanced infrared spectroscopy using metal oxide plasmonic antenna arrays. Nano Lett 14(1):346–352
6. Li L, Shuang FL, Puretzky AA et al (2012) Near-field enhanced ultraviolet resonance Raman spectroscopy using aluminum bow-tie nano-antenna. Appl Phys Lett 101(11):113116
7. Nielsen MG, Pors A, Albrektsen O, Bozhevolnyi SI (2012) Efficient absorption of visible radiation by gap plasmon resonators. Opt Express 20(12):13311–13319
8. Lyamkina AA, Schraml K, Regler A et al (2016) Monolithically integrated single quantum dots coupled to bowtie nanoantennas. Opt Express 24(25):28936–28944
9. Zeng C, Hu XG, Shi MJ et al (2016) Enhancing light emission from germanium quantum dots by bowtie antennas. J Lightwave Technol 34(14):3283–3287

10. Wang W, Zhang J, Che X et al (2016) Large absorption enhancement in ultrathin solar cells patterned by metallic nanocavity arrays. Sci Rep 6:34219
11. Lin L, Zheng Y (2015) Optimizing plasmonic nanoantennas via coordinated multiple coupling. Sci Rep 5:14788
12. Wuytens PC, Skirtach AG, Baets R (2017) On-chip surface-enhanced Raman spectroscopy using nanosphere-lithography patterned antennas on silicon nitride waveguides. Opt Express 25(11):12926–12934
13. Ding SY, Yi J, Li JF et al (2016) Nanostructure-based plasmon-enhanced Raman spectroscopy for surface analysis of materials. Nat Rev Mater 1(6):16021
14. Li WD, Ding F, Hu J et al (2011) Three-dimensional cavity nanoantenna coupled plasmonic nanodots for ultrahigh and uniform surface-enhanced Raman scattering over large area. Opt Express 19(5):3925–3936
15. Hatab NA, Hsueh CH, Gaddis AL, Retterer ST, Li JH, Eres G, Zhang Z, Gu B (2010) Free-standing optical gold bowtie nanoantenna with variable gap size for enhanced Raman spectroscopy. Nano Lett 10(12):4952–4955
16. Zhao C, Liu Y, Yang J, Zhang J (2014) Single-molecule detection and radiation control in solutions at high concentrations via a heterogeneous optical slot antenna. Nanoscale 6(15):9103–9109
17. Kinkhabwala A, Yu Z, Fan S et al (2009) Large single-molecule fluorescence enhancements produced by a bowtie nanoantenna. Nat Photonics 3(11):654–657
18. Lu G, Liu J, Zhang T, Shen H, Perriat P, Martini M, Tillement O, Gu Y, He Y, Wang Y, Gong Q (2013) Enhancing molecule fluorescence with asymmetrical plasmonic antennas. Nanoscale 5(14):6545–6551
19. McPhillips J, Murphy A, Jonsson MP, Hendren WR, Atkinson R, Höök F, Zayats AV, Pollard RJ (2010) High-performance biosensing using arrays of plasmonic nanotubes. ACS Nano 4(4):2210–2216
20. Spackova B, Wrobel P, Bockova M et al (2016) Optical biosensors based on plasmonic nanostructures: a review. Proc IEEE 104(12):2380–2408
21. Zhang C, Lu Y, Ni Y et al (2015) Plasmonic lasing of nanocavity embedding in metallic nanoantenna array. Nano Lett 15(2):1382–1387
22. Luo Y, Ahmadi ED, Shayan K et al (2017) Purcell-enhanced quantum yield from carbon nanotube excitons coupled to plasmonic nanocavities. Nat Commun 8(1):1413
23. Roxworthy BJ, Ko KD, Kumar A, Fung KH, Chow EK, Liu GL, Fang NX, Toussaint KC Jr (2012) Application of plasmonic bowtie nanoantenna arrays for optical trapping, stacking, and sorting. Nano Lett 12(2):796–801
24. Nie KY, Li J, Chen X, Xu Y, Tu X, Ren FF, du Q, Fu L, Kang L, Tang K, Gu S, Zhang R, Wu P, Zheng Y, Tan HH, Jagadish C, Ye J (2017) Extreme absorption enhancement in ZnTe:O/ZnO intermediate band core-shell nanowires by interplay of dielectric resonance and plasmonic bowtie nanoantennas. Sci Rep 7(1):7503
25. Lee B, Park J, Han GH, Ee HS, Naylor CH, Liu W, Johnson AT, Agarwal R (2015) Fano resonance and spectrally modified photoluminescence enhancement in monolayer MoS2 integrated with plasmonic nanoantenna array. Nano Lett 15(5):3646–3653
26. Gadalla MN, Abdel-Rahman M, Shamim A (2014) Design, optimization and fabrication of a 28.3 THz nano-rectenna for infrared detection and rectification. Sci Rep 4:4270
27. Weber D, Pablo A, Pablo AG et al (2011) Longitudinal and transverse coupling in infrared gold nanoantenna arrays: long range versus short range interaction regimes. Opt Express 19(16):15047–15061
28. Linnenbank H, Grynko Y, Förstner J et al (2016) Second harmonic generation spectroscopy on hybrid plasmonic/dielectric nanoantennas. Light: Sci Applic 5(1):e16013–e16013
29. Fischer H, Martin OJ (2008) Engineering the optical response of plasmonic nanoantennas. Opt Express 16(12):9144–9154
30. Savaliya PB, Thomas A, Dua R, Dhawan A (2017) Tunable optical switching in the near-infrared spectral regime by employing plasmonic nanoantennas containing phase change materials. Opt Express 25(20):23755–23772
31. Guo HC, Meyrath TP, Zentgraf T, Liu N, Fu L, Schweizer H, Giessen H (2008) Optical resonances of bowtie slot antennas and their geometry and material dependence. Opt Express 16(11):7756–7766
32. Mcfarland AD, Duyne RPV (2003) Single silver nanoparticles as real-time optical sensors with zeptomole sensitivity. Nano Lett 3(8):1057–1062
33. Shafer-Peltier KE, Haynes CL, Glucksberg MR, van Duyne R (2003) Toward a glucose biosensor based on surface-enhanced Raman scattering. J Am Chem Soc 125(2):588–593
34. Reed JC, Zhu H, Zhu AY, Li C, Cubukcu E (2012) Graphene-enabled silver nanoantenna sensors. Nano Lett 12(8):4090–4094
35. Naik GV (2013) Alternative plasmonic materials: beyond gold and silver. Adv Mater 25(24):3264–3294
36. Chowdhury MH, Krishanu R, Gray SK et al (2009) Aluminum nanoparticles as substrates for metal-enhanced fluorescence in the ultraviolet for the label-free detection of biomolecules. Anal Chem 81(4):1397–1403
37. Sigle DO, Perkins E, Baumberg JJ, Mahajan S (2013) Reproducible deep-UV SERRS on aluminum nanovoids. J Phys Chem Lett 4(9):1449–1452
38. Langhammer C, Schwind M, Kasemo B et al (2006) Localized surface plasmon resonances in aluminum nanodisks. Nano Lett 6(5):1461–1471
39. Mazzotta F, Wang G, Hägglund C et al (2011) Nanoplasmonic biosensing with on-chip electrical detection. Biosens Bioelectron 26(4):1131–1136
40. Li Z, Hattori HT, Lan F et al (2011) Merging photonic wire lasers and nanoantennas. J Lightwave Technol 29(18):2690–2697
41. Liu Z, Boltasseva A, Pedersen RH et al (2008) Plasmonic nanoantenna arrays for the visible. Metamaterials 2(1):45–51
42. Koenderink AF (2017) Single-photon nanoantennas. ACS Photonics 4(4):710–722
43. Rosen DA, Tao AR (2014) Modeling the optical properties of bowtie antenna generated by self-assembled Ag triangular nanoprisms. ACS Appl Mater Interfaces 6(6):4134–4142
44. Cao T, Wei CW, Simpson RE et al (2014) Broadband polarization-independent perfect absorber using a phasechange metamaterial at visible frequencies. Sci Rep 4:3955
45. Zijlstra P, Paulo PMR, Orrit M (2012) Optical detection of single non-absorbing molecules using the surface plasmon resonance of a gold nanorod. Nat Nanotechnol 7(6):379–382
46. Lee EK, Song JK, Jeong KY (2013) Design of plasmonic nanoantenna for total internal reflection fluorescence microscopy. Opt Express 21(20):23036
47. Baptiste A, Barnes WL (2008) Collective resonances in gold nanoparticle arrays. Phys Rev Lett 101(14):143902
48. Vecchi G, Giannini V, Rivas JG (2009) Shaping the fluorescent emission by lattice resonances in plasmonic crystals of nanoantennas. Phys Rev Lett 102(14):146807
49. Nordlander P, Prodan E (2004) Plasmon hybridization in nanoparticles near metallic surfaces. Nano Lett 4(11):2209–2213
50. Ding W, Bachelot R, Kostcheev S et al (2010) Surface plasmon resonances in silver bowtie nanoantennas with varied bow angles. J Appl Phys 108(12):124314
51. Ding W, Bachelot R, Lamaestre RED et al (2009) Understanding near/far-field engineering of optical dimer antennas through geometry modification. Opt Express 17:21228–21239
52. Novotny L (2007) Effective wavelength scaling for optical antennas. Phys Rev Lett 98(26):266802

53. Cialla D, März A, Böhme R, Theil F, Weber K, Schmitt M, Popp J (2012) Surface-enhanced Raman spectroscopy (SERS): progress and trends. Anal Bioanal Chem 403(1):27–54
54. Campion A, Kambhampati P (1998) Surface-enhanced Raman scattering. Chem Soc Rev 27(4):241
55. Yampolsky S, Fishman DA, Dey S et al (2014) Seeing a single molecule vibrate through time-resolved coherent anti-Stokes Raman scattering. Nat Photonics 8(8):650–656
56. Gupta N, Dhawan A (2018) Bridged-bowtie and cross bridged-bowtie nanohole arrays as SERS substrates with hotspot tunability and multi-wavelength SERS response. Opt Express 26(14):17899–17915
57. Jha SK, Ahmed Z, Agio M, Ekinci Y, Löffler JF (2012) Deep-UV surface-enhanced resonance Raman scattering of adenine on aluminum nanoparticle arrays. J Am Chem Soc 134(4):1966–1969
58. Ding SY, Yi J, Li J et al (2016) Nanostructure-based plasmon-enhanced Raman spectroscopy for surface analysis of materials. Nat Rev Mater 1:16021–16036
59. Zhang J, Irannejad M, Cui B (2014) Bowtie nanoantenna with single-digit nanometer gap for surface-enhanced Raman scattering (SERS). Plasmonics 10(4):831–837
60. Kaniber M (2016) Surface plasmon resonance spectroscopy of single bowtie nano-antennas using a differential reflectivity method. Sci Rep 6:23203
61. Singh SC, Zeng HB, Guo C et al (2012) Lasers: fundamentals, types, and operations. In: Nanomaterials: processing and characterization with lasers, 1rd edn. Wiley, New York, pp 1–34
62. Sreekanth KV, Alapan Y, ElKabbash M, Ilker E, Hinczewski M, Gurkan UA, de Luca A, Strangi G (2016) Extreme sensitivity biosensing platform based on hyperbolic metamaterials. Nat Mater 15(6):621–627
63. Rodrigo D, Limaj O, Janner D, Etezadi D, García de Abajo FJ, Pruneri V, Altug H (2015) Mid-infrared plasmonic biosensing with graphene. Science 349(6244):165–168
64. Singh SC, Zeng HB, Guo C et al (2012) Introduction of materials and architectures at the nanoscale. In: Nanomaterials: processing and characterization with lasers, 2rd edn. Wiley, New York, pp 35–65
65. Hill RT (2015) Plasmonic biosensors. Wires Nanomed Nanobiotechnol 7(2):152–168
66. Etezadi D, Warner Iv JB, Ruggeri FS et al (2017) Nanoplasmonic mid-infrared biosensor for in vitro protein secondary structure detection. Light: Sci Applic 6(8):e17029